Journal of Casting & Materials Engineering Vol. 8 No. 3 (2024) 30–44
https://doi.org/10.7494/jcme.2024.8.3.30

An Experimental Derivation of Transient Nonuniform External Boundary Conditions for the Solidification Process Modeling of Equiaxed Investment Castings

Weston Olson[a, b*], Michael Stemmler[b], Erik Fernandez[a], Jayanta Kapat[a]

[a] University of Central Florida, Center for Advanced Turbomachinery and Energy Research, 4000 Central Florida Blvd, Orlando, FL 32816
[b] Siemens Energy, Gas Services Central Large Gas Turbine Engineering, 11842 Corporate Blvd, Orlando, FL 32817
e-mail: weston.olson@siemens-energy.com

Received: 11 August 2024/Accepted: 4 September 2024/Published online: 30 September 2024.
This article is published with open access at AGH University of Science and Technology Journals.

Abstract

The external heat transfer mechanisms acting on the external mold surfaces for equiaxed casting processes are very complex. The mechanisms are multi-mode, transient, and nonuniform, consisting of very complex radiative and convective definitions. In this work, a real-life mold, SGT6-5000 FD 3/4 Blade 4 cast in Alloy-247, was instrumented with thermocouples and temperature readings were recorded throughout the entire casting sequence of events. Analytical models based on the first law of thermodynamics, Fourier's law, Newton's Law of Cooling, and diffuse gray radiation for an N-sided enclosure were developed to use the thermocouple data as input to back calculate the emissivity of the mold, as well as the spatially varying heat transfer coefficients for a number of local regions. The derived external heat transfer mechanisms are presented as transient Biot numbers. The derived emissivity and nonuniform heat transfer coefficients for these surfaces were then validated in ProCAST numerical simulation by comparing the external mold temperature profiles. An extensive iterative, curve fitting, extrapolating, and averaging procedure was exercised to derive an expression for emissivity across the entire temperature range associated with the casting process. The predicted temperatures on the nodes corresponding to the thermocouple locations agree within reasonable error with the experimental data. The model also qualitatively predicted the shrinkage porosity detected via x-ray imaging for this casting. The current study confirms the hypothesis of previous work by the current authors with respect to the transient nonuniform boundary condition concept. Unique values of heat transfer coefficients were observed at different vertical positions along the airfoil. The analytical models were also able to capture phenomena associated with specific sequences of the casting process. This work provides the analytical models, and procedure, needed to derive these spatially varying conditions. The current authors contribute to the intellectual know-how of the large gas turbine casting industry which by other foundries is considered highly proprietary and strictly confidential. This paper should be used to set the precedence for how foundries derive and validate the external boundary conditions used in solidification process modeling.

Keywords:

solidification process modeling, casting simulation, nickel-based superalloy, equiaxed investment casting, large gas turbine hardware, transient nonuniform heat transfer, initial condition natural convection, surface condition natural convection, mixed convection, rotational convection, ProCAST validation

1. INTRODUCTION

The external heat transfer coefficient and emissivity definition in solidification process modeling are parameters that are either over-looked or considered highly confidential within foundries. This work is an extension to the previous work of the current authors [1]. In the previous work, an extensive literature review was performed, and the correlations provided in the literature were used to define the transient nonuniform boundary conditions. Several assumptions were stated for justifying the application of these correlations. Although many assumptions were made in defining the external boundary conditions, the model predictions correlated well with the real-world data. The biggest inconsistency with the correlations found in the literature and the actual scenario was with respect to the initial condition. All the previous work found in the literature had an initial condition where the surface and ambient temperatures were the same, hence the surface and surrounding air heated up simultaneously. The actual scenario has an initial condition where the surface and ambient temperatures are not the same, a very hot surface is immediately exposed to cool ambient air. The next most critical inconsistency was with the surface condition, where all the correlations either used a constant surface temperature or constant

heat flux boundary condition. In investment casting no surface ever has a constant condition and one would expect different transient behavior in this scenario. Therefore, this work presents experimental data and analytical models which are validated numerically with the ProCAST FEA simulation package, which has an uncommon initial condition and a transient spatially varying surface condition.

It is known that the natural convection heat transfer coefficient depends on several geometrical, surface, and ambient parameters. The heat transfer coefficient associated with natural convection is arguably the most complex heat transfer mechanism for investment castings. The driving mechanism for natural convection are the buoyancy forces which are caused by the density gradient normal to the surface resulting from the temperature difference between the surface and the surrounding ambient air. With colder, heavier, and higher density, air molecules will drop under gravity and with hotter, lighter, and lower density, air molecules will rise. This bulk motion of air molecules dropping and rising is the buoyancy force which drives natural convection.

The reader is referred to Gebhart [2] for a conceptual overview of natural convection and its applications. The Grashof number [3] represents the ratio of buoyancy forces to viscous forces. This dimensionless number is proportional to the characteristic length by a power of three, Equation (1).

$$Gr_L = \frac{g\beta\left(T_s - T_\infty\right)L^3}{\nu^2} \tag{1}$$

where:

g – acceleration of gravity [m/s^2],
β – coefficient of thermal expansion [K^{-1}],
T_s – surface temperature [K],
T_∞ – ambient temperature [K],
L – characteristic length [m],
ν – kinematic viscosity [m^2/s].

The Grashof number is also one of the dependent variables for many natural convection Nusselt number correlations. The dependency is typically captured by the Rayleigh number which is simply the product of the Grashof number with the Prandtl number. In work by [1] several of these natural convection correlations are presented which are typically in the form of a coefficient multiplied by the Rayleigh number to some power. The coefficient and the power of the Rayleigh number are unique for each natural convection mechanism. The reader is referred to [1] for examples of these various Nusselt number correlations. Therefore, locally we expect to have a unique heat transfer coefficient for a unique characteristic length. Hence, the natural convection heat transfer coefficient will be a function of vertical height. Ostrach [4] was the first to obtain a numerical similarity solution to the coupled, nonlinear ordinary differential equations resulting in a correlation of Nusselt number as a function of Grashof number for various Prandtl numbers. The correlation is applicable to constant surface temperature laminar flow. Sparrow and Gregg [5] derived Nusselt number correlations by similarity solutions for a constant surface flux condition. They found that the Grashof number was proportional to the surface heat flux. Eckert [6] used an approximate integral solution for laminar flow over a constant temperature, vertical, and semi-infinite flat plate to derive the Nusselt number correlations. The derived correlations by [6] align very closely with those derived by [4]. Bayley [7] used a two-layer, laminar sublayer and a constant turbulent diffusivity layer temperature model to derive Nusselt number correlations for turbulent flow over a vertical, constant surface temperature, on a semi-infinite flat plate. Vliet and Ross [8] used experimental heat transfer data to develop a Nusselt number for constant surface heat flux condition for vertical and inclined plates. The vertical plate Nusselt number derived by [8] is almost identical to that derived by [7] for gases. Vliet and Ross [8] also uncovered some interesting phenomena with respect to the inclined plate. They concluded that the transition distance decreased for increasing angle with the vertical vector for unstable case (inclined upwards facing) and increased with increasing angle for stable case (inclined downwards facing). They found that the Nusselt number was independent of angle for the unstable case for angles up to 30 degrees and that for the stable case the gravity component should be modified by cosine square of the angle for angles up to 80 degrees. For the unstable case the buoyancy component is in the direction away from the surface and could lead to flow separation. The available literature is quite extensive and also covers horizontal cylinders [9–12], vertical cylinders [13–15], differently oriented cubes [16], and horizontal flat plates [17–19].

Another important convective mechanism which is applicable to the investment casting process is mixed free and forced convection. During the mold transfer from pre-heat oven to furnace, the mold is translating horizontally in space and may also be rotating right side up. Depending on the speed and size of the mold, mixed convection could certainly have an impact on mold temperature drop from mold transfer event to mold pouring event. This phenomenon has also been extensively investigated [20–28]. One thing all the previous work cited have in common is that the Nusselt number is a function of some characteristic length through the dependency on the Grashof number. Therefore, the current work seeks to define a relationship between the heat transfer coefficient and the characteristic length, specifically vertical height.

This work provides the guidelines of an experimental control volume energy balance analysis used to derive the transient spatially varying external heat transfer conditions for solidification process modeling. The experimental setup is defined in as much detail as permitted, due to intellectual property restrictions of the foundry. The derivation of the analytical models is then presented with detailed explanations on the mathematical manipulation of the governing equations. A thorough description on how to exercise the analytical models to derive physics driven boundary conditions for reliable solidification process modeling predictions is then discussed. Afterwards the results are described which illustrates the derived spatially varying external heat transfer conditions as transient Biot numbers before presenting the model prediction and real-world x-ray data comparisons. The paper then concludes with a summary of the phenomena uncovered by the analytical models and suggested topics which could serve as a continuation of this work.

2. EXPERIMENTAL SETUP

The casting setup, instrumentation, and process are discussed in this section. The experiment consisted of a 1x3 equiaxed SGT6-5000FD 3/4 blade 4 casting, which is gated from the bottom side of the root end face. The wax pattern assembly is illustrated in Figure 1. The instrumentation consisted of K-type thermocouples with a MicroDAQ battery powered data logger which recorded temperature values in intervals of 1 second. A temperature dependent error function was derived based on the thermocouple vendor specifications. The maximum reading error across the process temperatures was ~0.1%. Thermocouples were placed in-line vertically with three along the airfoil (TC1–3) and one on the side of the unmachined fur tree surface of the root (TC4), Figure 2. The wrapping scheme consisted of a three-step graded wrap along the airfoil with a single layer around root and gating. For each external thermocouple there was another thermocouple on the inside of the insulation layer perpendicular to the external thermocouple. This was done for the purpose of obtaining a volume average temperature and for an approximation on the heat transfer into the insulation layer through conductive mechanisms. More details with respect to this topic will be discussed in the following sections.

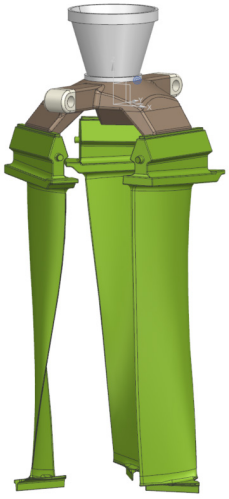

Fig. 1. Wax pattern assembly

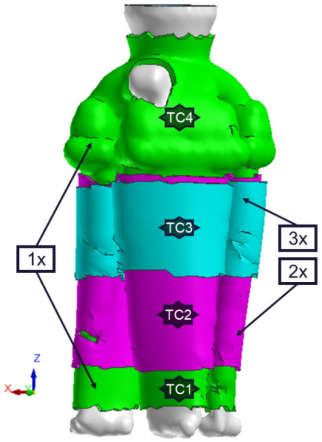

Fig. 2. Thermocouple location with wrapping scheme

The general sequence of events for the casting process are illustrated in Table 1. It should be noted that for this process event #5 was a whole order of magnitude greater in time than event #3. As the mold was transferred from the pre-heat oven to the furnace the data logger was also transferred to the furnace. The data logger began recording data before the pre-heat oven door was opened and continued recording until the mold was at room temperature. From this point on a data point will be defined as the resulting combined data of an external thermocouple with its corresponding internal thermocouple underneath the insulation wrapping. A step-by-step guide for an experimental setup with key notes is provided below:

- Define thermocouple placement based on spatially varying parameters (vertical position, curvature, angle/orientation, upward/downward facing, etc.). There should be at least one thermocouple placed in a region where its view factor with the surroundings is almost unity (this is needed for deriving the initial approximation for the emissivity).
- Create a complete data point by placing an internal thermocouple at a known distance perpendicular to the external thermocouple (for bare shell surfaces the interior thermocouple must be embedded into the shell).
- Have enough wiring to extend the wires through the pre-heat oven door to be connected to a battery powered data logger.
- Begin recording before pre-heat oven door opens for the mold transfer event #1. The battery powered data logger follows the mold throughout the entire casting process. Thermocouple data will be used to define the cooling rate of the control volumes, the external and internal temperatures, which are used as input to the analytical models.
- Take measurements of room temperature, surroundings, and interior furnace walls. These readings will be used to define the ambient and surrounding temperatures at which the mold exchanges heat with.
- Take note of the mechanism used to fix thermocouples to mold and its expected influence on the data.
- Take a video recording of the entire casting process to reference exact times for each sequence in Table 1. Event #1 consists of the mold flipping right side up, translating to the furnace, and securing the mold to the furnace fixture. The subevents which include motion will consist of mixed free and forced convection while the stationary subevent will consist of only free convection. The mixed convective phenomenon will be uncovered by the analytical model.

In general, the above step-by-step guide should suffice for most cases. There may need to be some modifications based on the specific constraints of certain foundries.

Table 1
Typical sequence of events for general investment casting process

#	Event
1	Mold transfer from pre-heat oven to furnace
2	Furnace pump down
3	Furnace vacuum hold
4	Mold fill
5	Furnace vacuum hold
6	Furnace vacuum break
7	Mold transfer from furnace to cooling zone
8	Alloy solidification in cooling zone

3. ANALYTICAL MODELS

The analytical models consist of an energy balance control volume analysis. The energy balance is defined by the first law of thermodynamics, Equation (2).

$$mC\frac{\partial T}{\partial t} = \dot{Q}_{in} - \dot{W}_{out} = \dot{Q}_{cond} - \dot{Q}_{conv} - \dot{Q}_{rad} - \dot{W}_{out} \tag{2}$$

where:

m – mass [kg],
C – specific heat [J/(kg · K)],
T – temperature [K],
t – time [s],
$\dot{Q}_{in}$ – rate of heat transfer into the system [W],
$\dot{Q}_{cond}$ – rate of conductive heat transfer [W],
$\dot{Q}_{conv}$ – rate of convective heat transfer [W],
$\dot{Q}_{rad}$ – rate of radiative heat transfer [W],
$\dot{W}_{out}$ – rate of work done by the system [W].

There is no work done on or by the system so the last term on the right-hand side of the equation goes to zero. The heat transfer into the system is a positive value, making the heat transfer out of the system a negative value. The heat transfer into the system is approximated as the conductive mechanism acting through the control volume. This mechanism is described by Fourier's Law, Equation (3). The heat transfer out of the system consists of convective and radiative mechanisms, which are described by Newton's Law of Cooling and diffuse gray radiation for an N-sided enclosure, respectively represented by Equations (4) and (5). It should be noted that representing the heat transfer into the control volume as the conduction acting through it is merely an approximation. This is a transient process and a portion of the heat transferred into the control volume is being stored. Therefore, this approximation is expected to give a larger estimate for the actual heat transfer into the control volume. It is a larger estimate since the temperature difference across the control volume would be less if there were no heat being stored. Hence, the temperature at the exterior of the control volume is the resulting temperature after the heat wave has transferred through the volume, with heat being stored along the way.

Fourier's Law which is a function of the thermal conductivity, cross sectional area, length across the control volume, and the temperature difference is illustrated by Equation (3).

$$\dot{Q}_{cond} = \frac{kA_c}{L}\left(T_i - T_e\right) \tag{3}$$

where:

k – thermal conductivity [W/(m · K)],
A_C – cross-sectional area [m^2],
L – length [m],
T_i – temperature of interior [K],
T_e – temperature of exterior [K].

Newton's Law of Cooling which is a function of the convective heat transfer coefficient, the wetted surface area, and the temperature difference is shown by Equation (4).

$$\dot{Q}_{conv} = hA_S\left(T_e - T_\infty\right) \tag{4}$$

where:

h – heat transfer coefficient [W/(m^2 · K)],
A_S – wetted surface area [m^2],
T_∞ – temperature of ambient air [K].

The diffuse gray radiation for an N-sided enclosure is depicted below, Equation (5). It is a function of the temperature, the emissivity, and the surface area of interest along with the view factor of that surface with all other surfaces it has a line of sight with. It also depends on the temperatures, emissivity, and surface area of those surfaces which have a line of sight with the surface of interest.

$$\dot{Q}_{rad} = \sum \frac{\sigma\left(T_j^4 - T_j^4\right)}{\frac{1-\varepsilon_j}{\varepsilon_j A_j} + \frac{1}{F_{j-k}A_j} + \frac{1-\varepsilon_k}{\varepsilon_k A_k}} \tag{5}$$

where:

σ – Stephan Boltzmann constant [W/(m^2 · K^4)],
A_j – wetted surface area of surface j [m^2],
A_k – wetted surface area of surface k [m^2],
T_j – temperature of surface j [K],
T_k – temperature of surface k [K],
ε_j – emissivity of surface j,
ε_k – emissivity of surface k,
$F_{j\text{-}k}$ – view factor from surface j to surface k.

Inserting Equations (3), (4,) and (5) into Equation (2) and rearranging it to solve the heat transfer coefficient gives Equation (6). All the parameters in Equation (6) are either obtained from the thermocouple data, are dimensional measurements, ambient parameters, or material properties of the control volume besides surface emissivity. The emissivity, as a function of temperature, of the external mold surface must be known before deriving a transient heat transfer coefficient definition. This relationship can be derived during the vacuum hold events (#3, 4, and 5) of the casting process. During these events, the convective mechanism is assumed to be zero, or close to zero.

$$h = \frac{\dot{Q}_{cond} - mC\frac{\partial T}{\partial t}}{A_S\left(T_e - T_\infty\right)} - \frac{\sum \frac{\sigma\left(T_e^4 - T_k^4\right)}{\frac{1-\varepsilon_e}{\varepsilon_e A_S} + \frac{1}{F_{e-k}A_S} + \frac{1-\varepsilon_k}{\varepsilon_k A_k}}}{A_S\left(T_e - T_\infty\right)} \tag{6}$$

where:

ε_e – emissivity of external data point,
$F_{e\text{-}k}$ – view factor from external data point to surface k.

Now we insert Equations (5) and (3) into Equation (2) and rearrange it to solve the emissivity issue which gives us

Equation (7). We now have one equation with one unknown, the one equation being Equation (6) and the unknown being the heat transfer coefficient. It should be noted that Equation (7) assumes radiation exchange is only between the data point and the furnace walls. It also assumes that the convection mechanism is zero. Therefore, the strategic placement of thermocouples is necessary for utilizing the proposed analytical models. The expression for the emissivity based on the assumption described above is shown below, Equation (7).

$$\varepsilon = \left[A_e \left(\frac{\sigma\left(T_e^4 - T_w^4\right)}{\dot{Q}_{cond} - mC\dfrac{\partial T}{\partial t}} - \frac{1}{F_{e-w}A_e} + \frac{1-\varepsilon_w}{\varepsilon_w A_w} \right) + 1 \right]^{-1} \tag{7}$$

where:

T_w – temperature of internal furnace walls [K],
ε_w – emissivity of internal furnace walls,
$F_{e\text{-}w}$ – view factor from external data point to internal furnace walls.

The analytical models are covered by Equations (6) and (7) and can be used to derive emissivity of insulation wraps and shell as well as the spatially varying heat transfer coefficients. The engineer using the analytical models must have an understanding of the assumptions and approximations. These include, but may not be limited to, the approximation that the heat transfer into the control volume is the conduction through the control volume, the negligible radiation between non furnace wall surfaces, the heat transfer coefficient is zero during vacuum hold events, and the impact on heat transfer from the mechanism used to fix the thermocouples to the mold.

4. TRANSIENT NONUNIFORM HEAT CONDITION DERIVATION

In this section, the procedure for exercising the analytical models is presented. The focus of this work is to derive the spatially varying heat transfer coefficients and to uncover phenomena associated with natural and mixed convection mechanisms for equiaxed investment casting processes. Therefore, the first thing that is needed is the emissivity of the external surface of the mold. This can be obtained from the use of Equation (7) or from a pyrometric camera.

If we are using Equation (7), the procedure consists of an extensive iterative, curve fitting, extrapolating, and averaging process. An initial estimate for the emissivity relationship with respect to temperature is the first requirement. Temperature dependent specific heat and thermal conductivity of the control volume must also be available. At each second, Equation (7) must be solved during the vacuum hold events (# 3, 4, and 5). The partial derivative of temperature with respect to time can simply be calculated by taking the derivative of the trendline through the volume averaged thermocouple data. The event time scales are sufficiently large and therefore a one second data rate is sufficient to adequately calculate the partial derivative. The control volume's volume was simply the thickness of the insulation layer multiplied by the surface area. The surface area was the suction-side chordwise span by approximately 38 mm since one of the objectives of the study was to observe phenomena associated with the heat transfer coefficient at various vertical positions.

The derived emissivity as a function of temperature should now be plotted across the temperature drop associated with the vacuum hold events. A trendline must be created through the data to derive a definition of emissivity as a function of temperature. There will not be any available raw data to derive the emissivity for higher and lower temperatures outside of vacuum hold events. Therefore, this function will be extrapolated to populate the missing data. Again, the purpose here is to derive an initial estimate for the emissivity knowing that the true emissivity may be somewhat different than the extrapolated expression. For this experiment data point TC4 was selected since this data point had the least amount of errors associated with the assumptions for the derivation of Equation (7). Figure 3 illustrates the normalized raw calculated data, with the best fit extrapolated trendline corresponding to the data, as a function of temperature. The temperature axis was normalized by the pre-heat temperature.

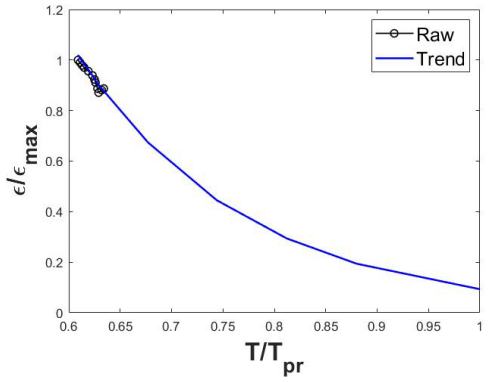

Fig. 3. Raw calculated emissivity and extrapolated trendline for TC4

Now that there is an initial expression for the emissivity, Equation (6) can be utilized to complete the definition of the external heat transfer mechanisms acting on the mold during all events. Iteration is required on the trendline type and curve fitting sections for the change of temperature with respect to time. Engineering judgement will help in selecting which trendlines best describe the event. For example, Equation (6) should have peaks during the mixed convection events. Therefore, a trendline for the change in temperature with respect to time should be selected which generates the desired parabolic profile for the heat transfer coefficient. The entire casting process will be divided into three separate simulations. Event #1 for the first simulation, events #2–5 for the second, and events #6–8 for the third. This allows for the necessary calibration of the emissivity, for relatively long vacuum holds, and heat transfer coefficients. The three simulations may be combined into a single simulation for short vacuum holds but caution should be used when applying the derived emissivity to models with longer vacuum holds. The dominating external heat transfer mechanism acting on the mold during the vacuum hold to this point is assumed to be radiation and it is highly dependent on emissivity. For the first simulation, the

combination of heat transfer coefficients with initial emissivity must be iterated on until the temperature profiles match the external data point within reasonable error. For this study an error of –10% to +10% was targeted. Further investigations are required to quantify the actual degree of process variation for this specific process.

For the second simulation Equation (7) is used for each data point to derive a unique expression for the emissivity. This is necessary if the emissivity is a piece-wise function with various functions at different temperature intervals. Recollection of the assumptions made on Equation (7) are necessary for making sense of the fine-tuned emissivity expressions for each data point during iterations. These external data points exchange radiation with different surfaces, so there will be errors in the raw calculation of Equation (7) for these data points. Therefore, unique expressions for emissivity are expected for each data point. Figure 4 illustrates the raw calculated and the calibrated normalized emissivity for each data point across the temperature ranges associated with the vacuum hold events, #3–5. The calibrated expressions have been extrapolated across the temperature scale.

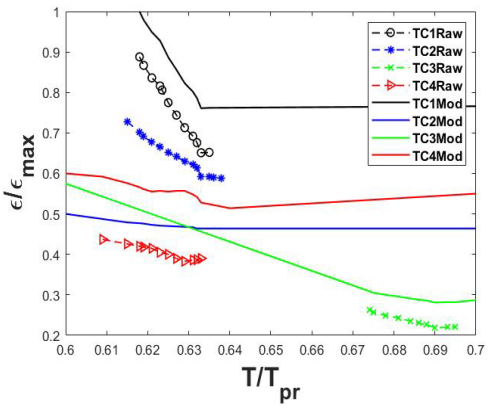

Fig. 4. Raw calculated emissivity and calibrated emissivity for all data points across temperature ranges associated with vacuum hold events

After the raw calculated emissivity from Equation (7) for each data point has been calibrated, an iterative, trendline fitting, extrapolating, and averaging procedure is needed to collapse all emissivity expressions, of insulation or shell material, into a single expression with use of Equation (8). Equation (8) is the same as Equation (7) with the addition of a convective mechanism. This removes the assumption of a zero convective mechanism during the "vacuum hold" events. The convective mechanism will be derived by Equation (6) and iterated simultaneously with the emissivity.

The modified form of Equation (7) is presented by Equation (8).

$$\varepsilon_e = \left[A_e \left(\frac{\sigma\left(T_e^4 - T_w^4\right)}{\dot{Q}_{cond} - mC\dfrac{\partial T}{\partial t} - \dot{Q}_{conv}} - \frac{1}{F_{e-w}A_e} + \frac{1-\varepsilon_w}{\varepsilon_w A_w} \right) + 1 \right]^{-1} \quad (8)$$

Engineering judgement must be practiced for defining the expression of emissivity for temperatures outside of the temperature range of events #3–5. For example, the combination of conductive, convective, and radiative terms must be equivalent to the change in internal energy and non-negative values. A key tip is provided regarding the profile transition illustrated for all data points. All the raw calculated data points illustrated a transition point in their profiles, each occurring at different temperatures. This implies that each data point has unique heat transfer mechanisms acting on them. The profiles of each piecewise function were averaged for all data points and the transition temperature, which connects the two piecewise functions, was iterated on until the predicted model temperatures matched the experimental thermocouple data. This derived expression can now be used in Equation (6) for all casting events. The final calibrated emissivity which results in a best fit in predicted temperatures for all the data points across all temperatures is illustrated in Figure 5. Equation (6) must be used again with the final expression of emissivity across all casting events. The process for deriving the emissivity by Equations (7) and (8) can be very difficult and time consuming. With use of a pyrometric camera the time and effort in defining the external boundary conditions could possibly be reduced.

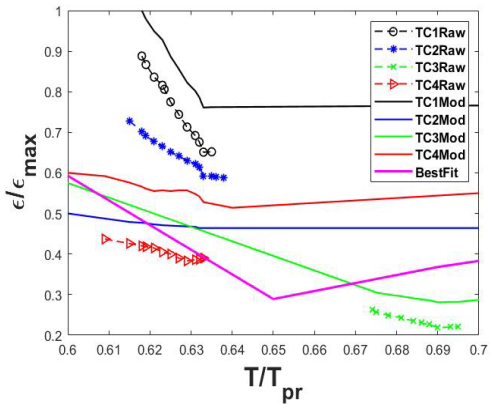

Fig. 5. Best fit emissivity relationship for all data points across all temperatures

A high-level summary of the procedure is provided below:

- Use Equation (7) for events #3, 4, and 5 to derive an extrapolated initial estimate for emissivity.
- Use Equation (6), with extrapolated initial emissivity, for events #1 and 2 in an iterative trendline, curve fitting process until all data points are within an acceptable targeted deviation.
- Use Equation (8) for all data points with an iterative trendline, curve fitting, averaging, extrapolating procedure to collapse all emissivity expressions into a single expression which best fits all the temperature data.
- Use the collapsed emissivity expression in Equation (6) to derive local transient spatially varying heat transfer coefficients across all casting events.

5. RESULTS AND DISCUSSION

The results consist of presenting the time dependent temperature profiles of the external thermocouple readings overlapped with the ProCAST predicted temperatures. Separate plots for each data point will be presented for events #1, 2, 3–5, and 6–8.

Each event for each plot is separated by a vertical dash dot line. The transient spatially varying external boundary conditions, which consist of the emissivity combined with the heat transfer coefficient, are presented as the Biot number. Typically, the Biot number is the ratio of conductive heat resistance to convective heat resistance. In this work the Biot number will represent the ratio of internal heat resistance to external heat resistance, where the external heat resistance is the combination of convective and radiative heat resistances. Equation (9) represents the Biot number and Equation 10 represents the radiative conductance. It should be noted that Equation (9) represents the external heat resistance associated with the ambient surroundings. The radiative heat transfer with other surfaces not being the ambient surroundings is not considered in this expression.

The total external resistance Biot number is shown by Equation (9).

$$Bi = \frac{\left(h_{conv} + h_{rad}\right) L_v}{k_v} \tag{9}$$

where:

h_{conv} – convective heat transfer coefficient [W/(m^2 · K)],
h_{rad} – radiative conductance [W/(m^2 · K)],
L_V – thickness of control volume [m],
k_V – thermal conductivity of control volume [W/(m · K)].

The radiative conductance described in Equation (10) is illustrated below.

$$h_{rad} = \varepsilon_e \sigma F_{e-w} \left(T_e^2 + T_w^2\right)\left(T_e - T_w\right) \tag{10}$$

The Biot number for each data point will be plotted as a function of time for events #1, 2, 3–5, and 6–8. Explanations on the convective phenomena associated with each event will be discussed and reference will be placed on time dependent plots for the traditional Biot number, which is Equation (9) without the radiative conductance term. Both forms of the Biot number will be analyzed to qualitatively evaluate the total external heat resistance, convective plus radiative, as well as the isolated convective resistance. To make physics-based explanations on the local phenomena, the ProCAST model was used to output the local time dependent solid fractions of the alloy corresponding to the data point locations in combination with reference to the temperature dependent specific enthalpy of the alloy. Finally, the model shrinkage porosity predictions will be compared to real-world x-ray results.

The time dependent temperature profiles for each data point for casting events #1 and 2 are illustrated in Figure 6. The time axis is normalized by the time associated with the corresponding events and the temperature axis is normalized by the pre-heat temperature. Data point TC3 slightly falls out of the targeted 10% for a portion of events #1 and 2 but comes back in within the targeted deviation before the end of event #2. This deviation is acceptable since the temperature of the mold is most critical while it is filled with the alloy. For this reason, the iterative trendline curve fitting procedure was not used to calibrate the derived heat transfer coefficient further to better match the temperature results.

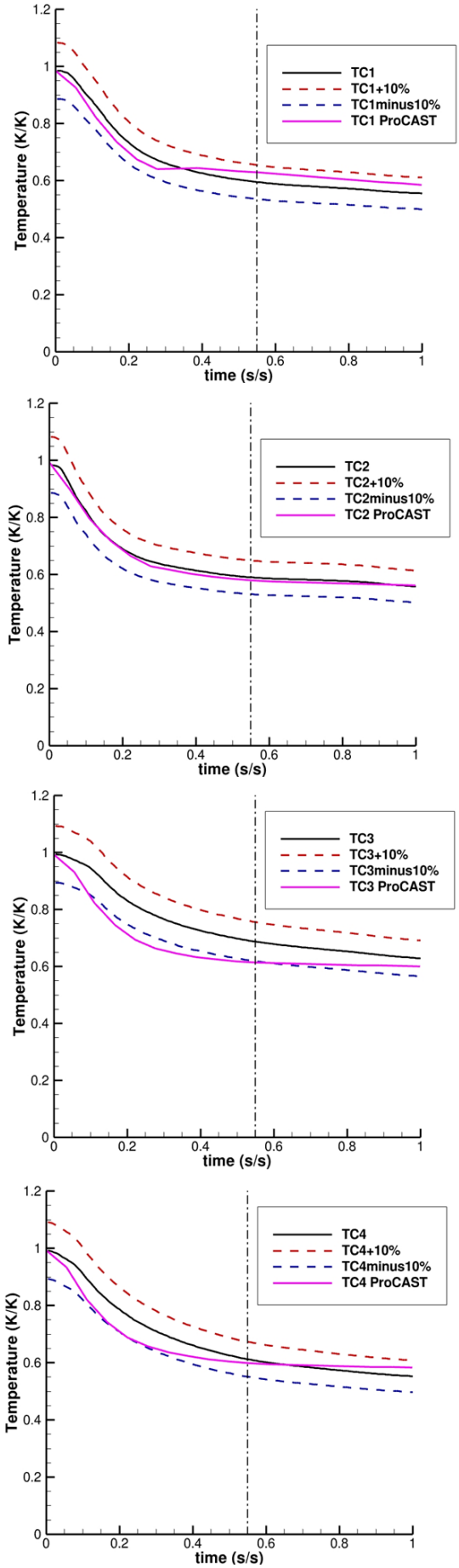

Fig. 6. Time dependent temperature profiles for events #1 and 2

The convective plus radiative Biot number is shown in Figure 7. The main distinction between the data points is with the initial values of total external resistance Biot number. This can be explained by the influence of the radiative conductance. The radiative conductance will be maximum for data point TC4 since its view factor is unity. As we move from data point TC4 to data point TC1 the view factors with the surroundings for each data point will decrease as the view factor with the tip shroud becomes more prominent. Figure 8 illustrates the convective Biot number to isolate the convective mechanism and analyze the transient nonuniform heat transfer coefficient. If we refer to Equation (1), we expect that the data points with a higher vertical position to have a higher heat transfer coefficient.

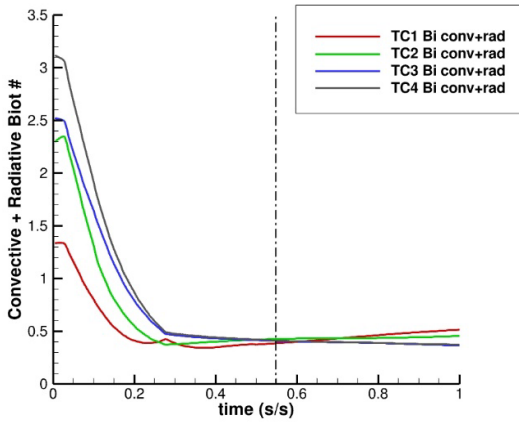

Fig. 7. Time dependent convective plus radiative Biot number profiles for events #1 and 2

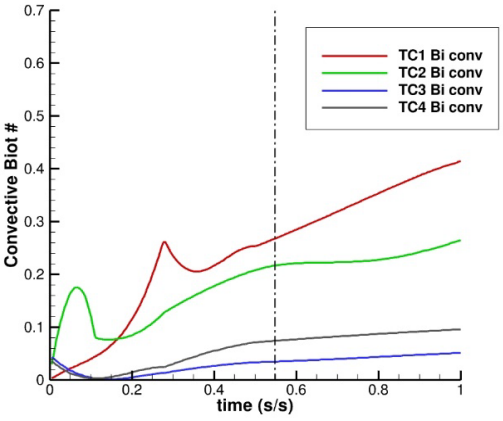

Fig. 8. Time dependent convective Biot number profiles for events #1 and 2

Consideration must be placed on the fact that the mold is in motion during a portion event #1, with a time corresponding to the dimensionless time of approximately 0–0.3. With this consideration we know that there will be a mixed convective mechanism acting on the mold. This casting was loaded in the pre-heat oven pour cup down. This fact also provides another explanation for the Biot number relationship illustrated in Figure 7. As the pre-heat oven door opens vertically, the data points which begin exchanging radiation with the cooler surroundings will initially have a higher radiative conductance. The motion during event #1 consists of translation (movement from pre-heat oven to furnace) plus rotation (flipping the mold right-side up), Figure (9). The rotational velocity is described by Equation (11):

$$V_{\omega} = R_{TC} \times \omega \tag{11}$$

where:

R_{TC} – rotational arm [m],
ω – rotational speed [revolutions/s].

Figure 9 illustrates the two forced convection mechanisms associated with the mold transfer event. Since data point TC1 has the largest rotational arm, it will have the largest rotational velocity and in return the highest heat transfer coefficient corresponding to the mold transfer event #1. Another motion not illustrated in Figure 9 is a 180-degree rotation about a nonstationary vertical axis. The mold transfer was done manually, and the rotational speeds were not constant. This explains why data point TC2 peaks before TC1. Further evaluation of Figure 8 illustrates a higher rate of increase in heat transfer coefficient for data point TC1. The increase in rate of heat transfer coefficient can be qualitatively described by the slope of the curves in Figure 8. This suggests that there are some other underlying phenomena. The reasoning for this behavior is as follows. The mold is stationary after a normalized time of approximately 0.3 and is only experiencing natural convection. The mold will be radiating large amounts of heat to the fixture it rests upon as well as the shelled tip shroud. The upper surface of the fixture, which is one of the surfaces closest to data point TC1 will heat up. Upon doing so the upper surface of the fixture will also experience natural convection. The lower density air molecules traveling upwards will add another natural convective component on data point TC1. Data point TC1 is therefore experiencing buoyancy driven forces from its own surface combined with the horizontal surfaces below it. The analytical models were able to uncover the mixed convective phenomena associated with the rotation of the mold during mold transfer. They also uncovered natural convective phenomena regarding the interaction of buoyancy forces between data point TC1 and the horizontal surfaces below it.

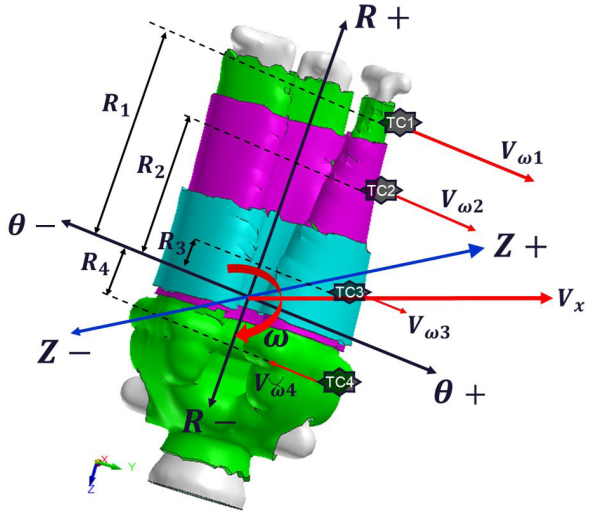

Fig. 9. Forced convection mechanisms acting on mold during event #1

For events #3–5, the time dependent temperature plots are shown in Figure 10. All the predicted temperatures fall within the targeted deviation of around 10%. Figures 11 and 12 represent the convective plus radiative Biot number and the convective Biot number, respectively. Events #3–5 are the vacuum hold events. It should be noted that no industrial furnace can achieve 100% vacuum. There will always be some percentage of air in the furnace. This trial was run in a medium grade furnace thus it is expected that there be some portion of air remaining in the furnace.

Referring to Figure 12, it is observed that the slope of data point TC4 is the highest and data point TC1 is second highest. The slopes of data points TC2 and TC3 are comparable. Again, referring to Equation (1) it is expected that the data points with the highest vertical position would experience the highest heat transfer coefficient. Let's refer to Figure 2 for reference to the wrapping scheme to explain the phenomenon which the analytical models have uncovered. Data points TC1 and TC4 have a single layer of insulation, while data points TC2 and TC3 have two and three layers, respectively. This implies that the natural convection heat transfer coefficient for equiaxed investment casted molds depends on the number of insulation wraps. This also agrees with findings by [5] where it was concluded that the Grashof number was proportional to the surface heat flux.

Therefore, it is expected that the more insulation layers, the lesser the surface heat flux and in return the lesser the buoyancy forces which drive the heat transfer coefficient. Data point TC4 increases at a greater rate than data point TC1 because it is at a higher vertical position and which agrees with the evaluation of Equation (1). Data points TC2 and TC3 are comparable because data point TC3 is at a higher vertical height and has an additional layer of insulation.

The magnitude of the heat transfer coefficients is questionable since one would assume that under vacuum, or a partial vacuum for this case, the heat transfer coefficients would be less in comparison to the non-vacuum events. The following explanation for this phenomenon is purely an assumption and requires extensive investigation for validation. The air molecules surrounding the mold are under buoyancy forces which create a resistance to the pump down. The air molecules far away from the mold are stagnant and provide no resistance to the pump down. Hence, during the pump down and vacuum hold events there is a sheet of air molecules surrounding the mold which are driven by the buoyancy forces. Again, this is purely an assumption which, to the best knowledge of the current authors, no previous studies have yet considered. Investigating this phenomenon can serve as a continuation of the current work. This results in the increase in heat transfer coefficient during these events. An additional phenomenon driving the increase in heat transfer coefficient during event #5, which corresponds to a nondimensional time of approximately 0.1–1.0, is that the mold is now filled with alloy. As the alloy begins to solidify, it releases energy in the form of heat into the mold. This additional heat flux is depicted by the transition in slopes of the curves at the dimensionless time of approximately 0.1 in Figure 12. For events #3–5 the analytical models uncovered that the heat transfer coefficient depends on the number of insulation layers, the energy released by the alloy during solidification, and another phenomenon which requires further investigation.

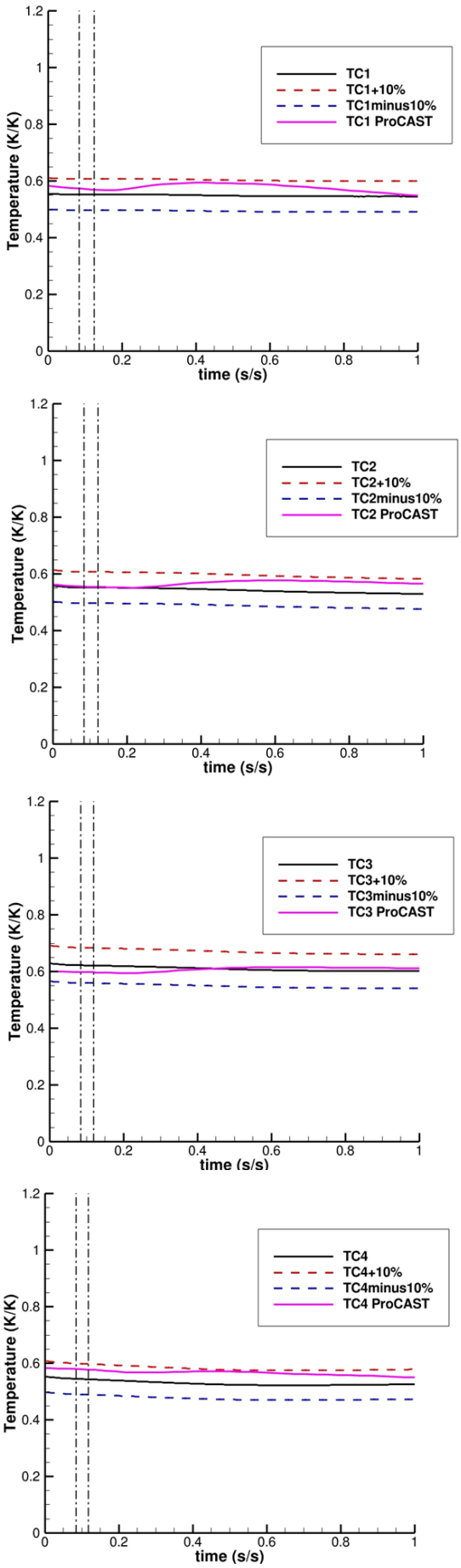

Fig. 10. Time dependent temperature profiles for events #3–5

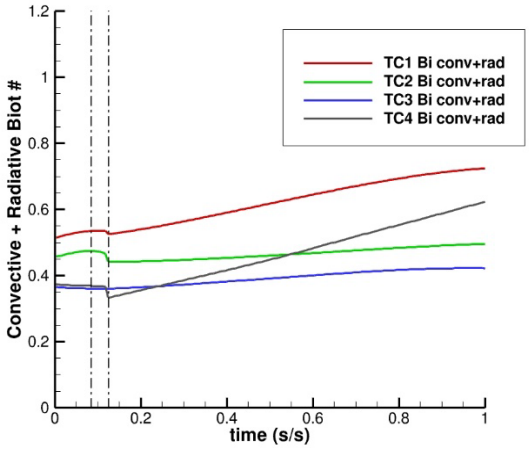

Fig. 11. Time dependent convective plus radiative Biot number profiles for events #3–5

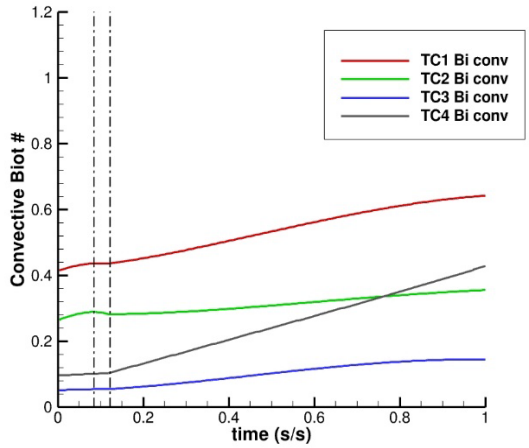

Fig. 12. Time dependent convective Biot number profiles for events #3–5

Figure 13 shows the time dependent normalized temperature profiles for events #6–8. The predicted temperature profiles agree exceptionally well with the experimental data. The analytical models have been successful in defining the boundary conditions on the exterior mold surfaces, for this case was the insulation wrapping, to match the experimental data within the targeted 10%. The experimental temperature profiles for data points TC3 and TC4 illustrate a small bump in temperature at approximately a dimensionless time of 0.55. This bump in temperature will be explained shortly. It should be noted that it is the combination of emissivity and heat transfer coefficient which define the proper external conditions. There may be some deviation in the actual values of these properties and the emissivity should be validated by pyrometry measurements. If pyrometry measurements show a difference in the derived emissivity from the procedure outlined in Section 4 of this work, then the emissivity resulting from the pyrometry analysis should be used in Equation (6) to calibrate the derived heat transfer coefficients. The time dependent temperature profiles were the result of an extensive amount of effort working with the analytical models.

The convective plus radiative Biot number profiles derived by the analytical models can be seen in Figure 14. The plot also illustrates small bumps in the Biot number at approximately the same instance in time for data points TC3 and TC4.

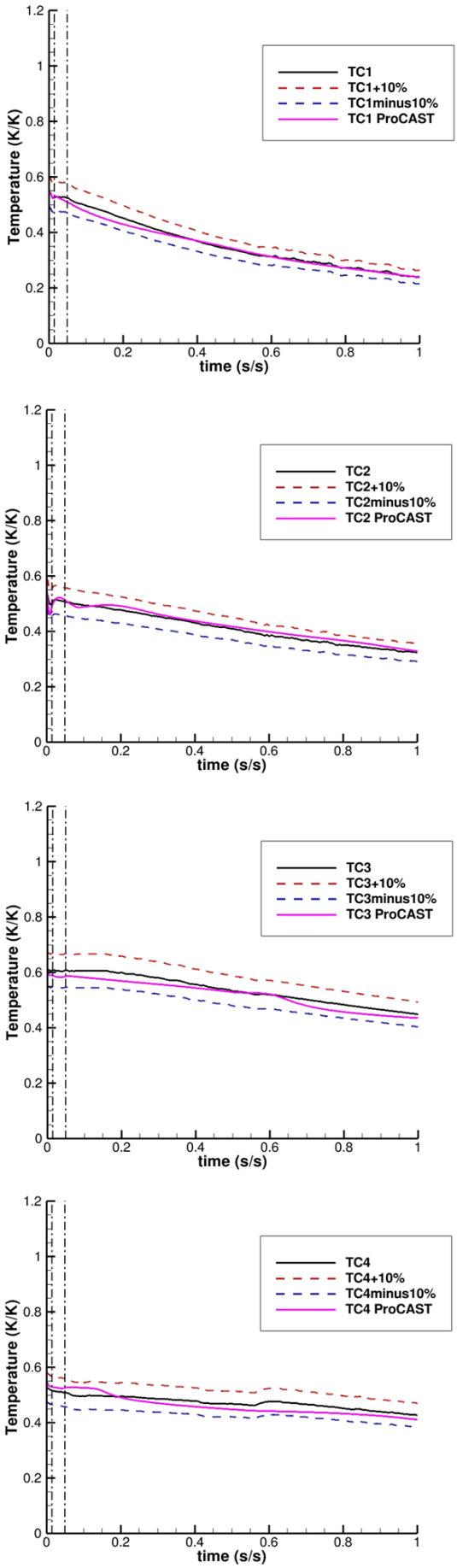

Fig. 13. Time dependent temperature profiles for events #6–8

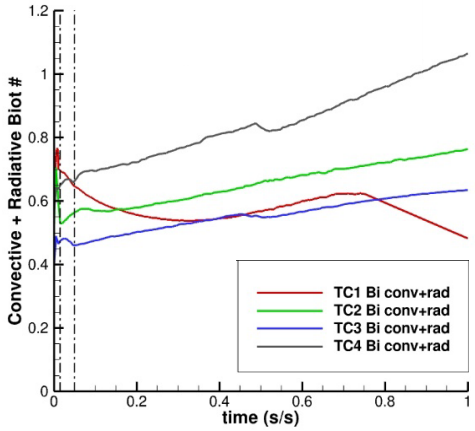

Fig. 14. Time dependent convective plus radiative Biot number profiles for events #6–8

The peaks at the very beginning of the profiles corresponds to the vacuum break period, event #6. The profiles also illustrate a secondary, shallower, peak after the vacuum break. This represents event #7 where the furnace door has opened, and the mold has been transferred to the cooling zone. The analytical models were able to capture the transition in surrounding conditions associated with the radiative mechanism. Data point TC1 experiences a decrease in Biot number at a dimensionless time of approximately 0.8. This implies that the conductive mechanism is becoming dominant over the two external mechanisms, convection and radiation, but this isn't expected for Biot numbers greater than 0.01. This suggests that there is another phenomenon yet to be discovered.

The convective Biot number, which isolates the convective mechanisms, is illustrated in Figure 15. The vacuum break is depicted by the initial peaks in the profiles. For this event, #6, there is a surge of ambient air which is re-introduced into the furnace. The convective mechanism at this event is a mixed convection mechanism, forced plus natural. Data point TC2 has the largest peak, followed by data point TC1. The peaks of data points TC3 and TC4 are comparable. This phenomenon implies that the magnitude of the forced convection component depends on the local surface position with respect to the furnace vents. Data point TC1 was slightly shielded by the fixture which the mold rests upon and data point TC2 was most exposed to the surge of air entering the furnace.

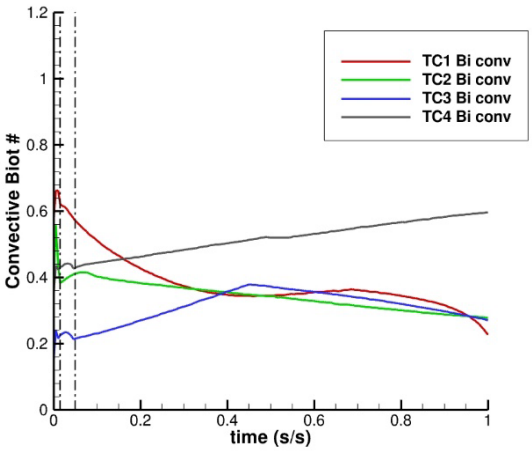

Fig. 15. Time dependent convective Biot number profiles for events #6–8

The secondary, shallower, peak is also illustrated in this plot. This event, #7, also consists of a mixed convection mechanism. In contrast to the previous event, where the forced convection component consisted of the surge of air entering the furnace, the forced convection component for event #6 is driven by the translation motion of the mold transferring to the cooling zone. During the last event in the casting process, event #8, the convective mechanism consists solely of natural convection. During this event, which begins at a dimensionless time of approximately 0.1, all the data points illustrate unique behaviors. Data point TC1 and TC2 are decreasing, with TC1 being more drastic, data point TC3 shows the greatest increase in convective Biot number with a change in direction at a dimensionless time of approximately 0.5, data point TC4 illustrates a continuous increase with a small bump corresponding to the same time in which TC3 transitions in the slope direction.

According to the natural convection phenomenon uncovered in the previous casting events analyzed, one would expect to see different behaviors. At this point we will summarize the discovered and validated phenomenon. The phenomenon validated is that the heat transfer coefficients depend on surface heat flux, which is controlled by number of insulation layers, and vertical position along the mold. The phenomenon discovered is the secondary flow of combined buoyancy forces for surfaces closest to the fixture or other horizontal surfaces, and whether the mold is filled with an alloy which provides an additional heat flux. Further investigation of the latter is now presented.

The alloy will be releasing energy in the form of heat to the mold. In return this heat will be transferred to the external surface of the mold where it exchanges heat with the ambient surroundings. This heat, released by the alloy, can be quantified by the rate of change in alloy specific enthalpy multiplied by the local mass of the alloy. The temperature dependent specific enthalpy of the alloy is shown in Figure 16. The temperature axis is normalized by the liquidus temperature of the alloy. The temperature dependent specific enthalpy was computed by the ProCAST internal CompuTHERM module. The vertical blue and red lines represent the solidus and liquidus temperatures, respectively. From analysis of Figure 16 the slope of the specific enthalpy is much steeper in the mushy zone, which is the zone between the solidus and liquidus temperatures. Hence, the heat being released by the alloy will be much greater while it is in the mushy phase.

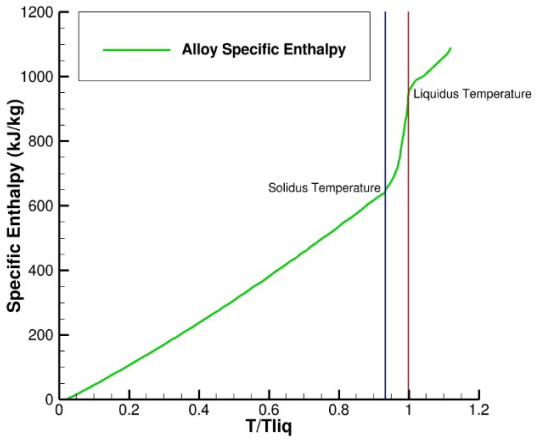

Fig. 16. Temperature dependent specific enthalpy derived by CompuTHERM

To draw some conclusions to the behaviors illustrated in Figure 15 we refer to the predicted time dependent solid fraction plots, Figure 17. At these events, #6–8, the local alloy corresponding to data point TC1 has already been completely solidified. The change in specific enthalpy in the solid phase is much less than that of the mushy phase. This results in less heat flux being transferred to the surface corresponding to the location of data point TC1. The vertical position of this data point is also the lowest, which contributes to the drastic decrease in natural convection.

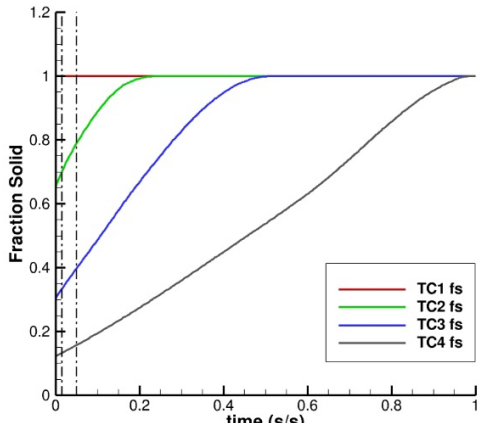

Fig. 17. Time dependent solid fraction predictions

At approximately the dimensionless time of 0.5, the convective Biot number begins to increase and then drops back down at a dimensionless time of 0.7. This can be explained by the temperature dependent thermal conductivity of the insulation layer, which is shown in Figure 18. Referring to Figure 13 data point TC1 has the lowest temperature which will result in the lowest thermal conductivity of all data points. The rate of decrease in thermal conductivity for this data point, which is defined by the thermal diffusivity, is greater than the rate of decrease in the natural convection heat transfer coefficient. This results in a temporary increase in convective Biot number illustrated in Figure 15. The rate in decrease of heat transfer coefficient than overcomes the rate of decrease in thermal conductivity after the internal energy of the control volume has decreased due to the thermal diffusivity. This conclusion was drawn by referencing the quantitative behavior of actual transient heat transfer coefficient. The quantitative values of heat transfer coefficient are not presented in this work due to intellectual property restrictions. The quantitative distribution of heat transfer coefficient does not illustrate any increase in heat transfer coefficient during this event. This phenomenon suggests that the heat transfer coefficient is also dependent on the thermal diffusivity of the control volume of the external mold surface which is driven by the rate of change in alloy specific enthalpy.

The rate of decrease of data point TC2 suggests that the heat flux at the surface is decreasing which makes sense from evaluation of Figure 17. The local alloy corresponding to this data point is still in the mushy phase up until a dimensionless time of approximately 0.2. This explains why the decrease in rate is less than data point TC1 and the fact that this data point has a higher vertical position. Recall that this data point has an additional layer of insulation which is expected to have an increased influence on the decrease in heat transfer coefficient with respect to data point TC1. One would expect that after the dimensionless time of approximate 0.7, where both data points TC1 and TC2 are well solidified, this data point would have a more comparable rate of decrease in heat transfer coefficient. One could argue that the heat transfer coefficient dependence on vertical height is greater than that of the surface flux or there is another underlying phenomenon yet to be uncovered.

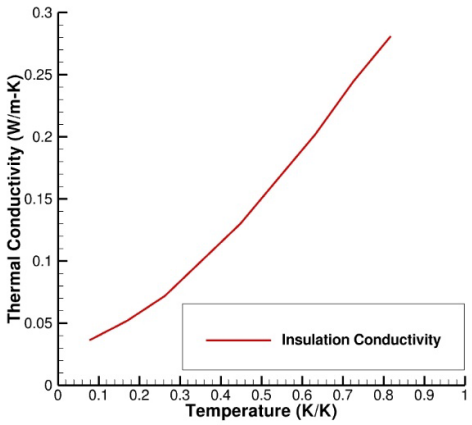

Fig. 18. Temperature dependent thermal conductivity of insulation layer

This could be explained by reference to the local mass of both data points TC1 and TC2. When traveling up the airfoil from tip to root, the local mass increases. The local mass of data point TC2 is greater than that of TC1 which results in a larger amount of heat being released locally since the heat is quantified by the rate of change in specific enthalpy multiplied by the local mass. Therefore, if the local alloy of both data points had the same temperature and the same cooling rate the data point corresponding to the larger local alloy mass would give off more heat. The analysis of comparing both data points TC1 and TC2 suggests that there is a phenomenon which relates the local heat transfer coefficient to the local mass of the alloy.

An increase in heat transfer coefficient followed by a decrease in heat transfer coefficient at the dimensionless time of approximately 0.5 describes the behavior of data point TC3 for event #8. The rate of increase in heat transfer is greater for this data point than for data point TC4. If we evaluate Figure 13 closely it is seen that the predicted temperature for data point TC3, which is driven by the derived boundary conditions presented in the Biot number plots, has a slightly greater cooling rate in comparison to the experimental data. This proposes that the trendline curve fitting procedure outlined in Section 4 requires further calibration. This proposal also agrees with the previous phenomena uncovered until now which would suggest that data point TC4 have the highest increase in rate of heat transfer coefficient since it has the highest vertical position, a single layer of insulation, has the lowest level of solid fraction, and has the highest mass. The change in direction of heat transfer coefficient rate at the dimensionless time of approximately 0.5 for data point TC3 can be explained by analyzing the behavior of this data point in Figure 17. At approximately this same point in time is when the local mass corresponding to this data point has reached complete solidification. Again, from Figure 16 it is shown that there is a drastic decrease in slope magnitude for the specific enthalpy of the alloy once it reaches the solid phase.

This means that there is a phenomenon which creates a dependency on the heat transfer coefficient to the mushy-solid phase transition of the alloy. After this transition at a nondimensional time of approximately 0.5 to 0.9 the magnitude of the heat transfer coefficient is greater than that of data point TC2. Which aligns with the previous phenomena uncovered, and validated, with respect to vertical position, local specific enthalpy, and local mass. The rate of decrease in heat transfer coefficient is greater for this data point, TC3, in comparison to data point TC2. This also aligns with the phenomenon which gives a relationship between the heat transfer coefficient and the number of insulation layers.

Data point TC4 illustrates a continuous increase in heat transfer coefficient with a greater magnitude in comparison to the other data points for the majority of event #8. This relationship is expected since it has the highest vertical position of all the data points and implies that there is phenomenon which create a dependency of the heat transfer coefficient with the number of insulation layers, the local specific enthalpy of the alloy, and the local mass of the alloy. The time dependent relationship for this data point, TC4, in Figure 15 illustrates a small peak in the profile at a dimensionless time of approximately 0.5. The fraction solid relationship of this data point is essentially in the mushy zone during this entire event, #8. Further investigation of the mushy zone specific enthalpy will give insight on this phenomenon. Figure 19 illustrates the specific enthalpy across the mushy zone normalized temperatures. There appears to be a change in the temperature dependent profile of the specific enthalpy at the normalized temperature of approximately 0.98. This temperature is represented by the magenta-colored vertical line. The predicted time dependent local alloy temperature corresponding to this data point is illustrated in Figure 20. The temperature axis has been normalized by the liquidus temperature. After evaluation of the time dependent local alloy temperature, it is observed that the local alloy temperature at the same time the convective Biot number illustrates a small peak corresponds to the same temperature at which the specific enthalpies temperature profile changes, represented by the horizontal dashed line. Another phenomenon uncovered by the analytical models implies that the heat transfer coefficient also depends on a change in the temperature dependent profiles of specific enthalpy in the mushy zone.

An extensive, thorough evaluation of the nonuniform spatially varying heat transfer coefficients through use of the analytical models presented in Section 3 have uncovered numerous convective phenomena associated with equiaxed investment casting processes, which are assumed to have been overlooked by foundries in the investment casting industry. The hypothesis that the heat transfer coefficient varies locally across the external surface of the mold presented by the current others in the previous work [1] has been validated in this work. It is extremely imperative that appropriate boundary conditions are defined in the casting simulation model to provide reliable predictions. The temperature gradient through the mold will not be reliably predicted if the external conditions on the mold are not accurately defined. This could result in serious consequences on the validity of the model predictions. The results and discussion section of this work will conclude by first presenting the x-ray image associated with this casting followed by the model predictions. The model predictions consist of evaluating the fraction solid and total shrinkage porosity results.

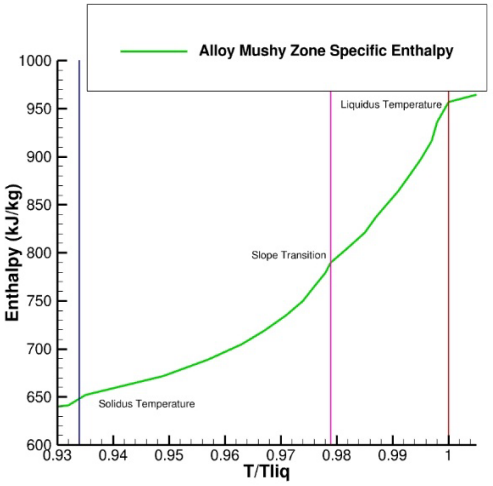

Fig. 19. Temperature dependent specific enthalpy across the mushy zone derived by CompuTHERM

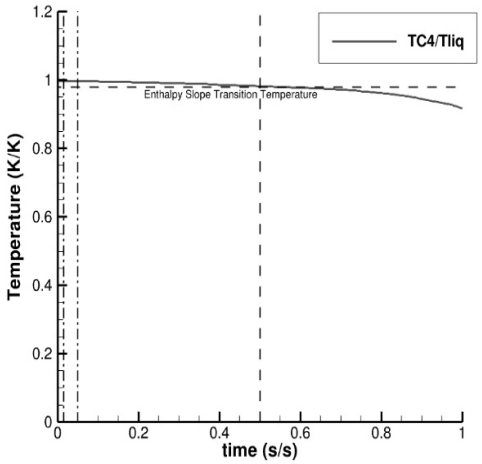

Fig. 20. Predicted time dependent local normalized alloy temperature for data point TC4

The x-ray image is shown in Figure 21. The x-ray inspection detected two areas of sponge shrink. A large area in the lower portion of the airfoil towards the root and another smaller region in the airfoil fillet. The x-ray inspector is trained and experienced in detecting shrink via x-ray inspection. To the untrained eye it is difficult to determine where the shrink is. For solid castings it is easier to detect in comparison to cored castings. The regions of shrink appear as shadows, or darker shades of gray, in comparison to regions next to it. Several patches of sponge shrink are highlighted by circles in Figure 21.

The fraction solid model predictions are shown in Figure 22. There is a large, isolated region of fraction solid in the lower portion of the airfoil corresponding to the same location where the x-ray inspection detected the shrinkage porosity. Isolated regions of fraction solid indicate that inter-dendritic liquid feeding has been cut-off to the isolated regions since the surroundings have already solidified past the critical fraction solid value. For this analysis that value was 0.7 and corresponds to the default value of the ProCAST simulation parameter "MACROFS".

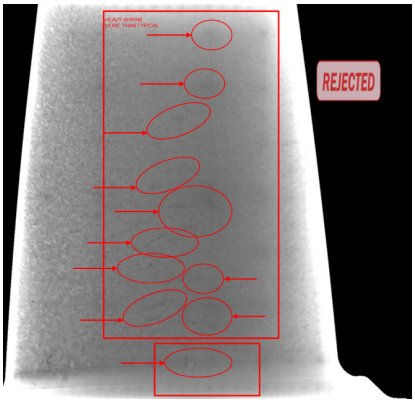

Fig. 21. X-ray image highlighting detectable shrinkage porosity

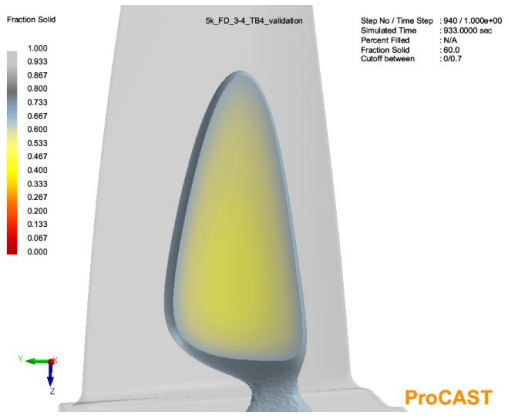

Fig. 22. Isolated region of fraction solid ProCAST model predictions

The critical fraction solid value is another subject which requires an extensive investigation for derivation. To the best of the authors knowledge, there are no studies which have researched this characteristic or its dependencies. It is assumed that the value most certainly depends on the alloy properties in the mushy zone and perhaps also depends on specific details of the geometry such as wall thickness distributions. The total shrinkage porosity model prediction is shown in Figure 23.

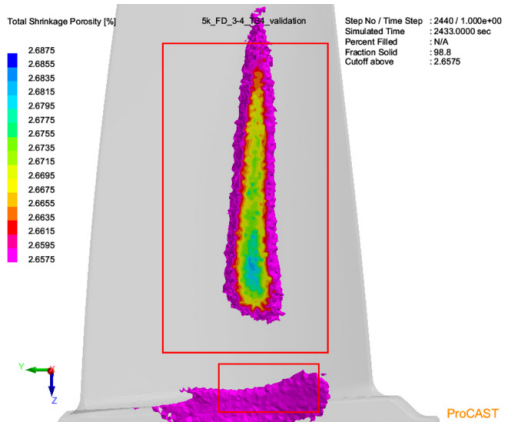

Fig. 23. Total shrinkage porosity ProCAST model predictions

The model was able to predict the two regions detected by the x-ray inspection at essentially the exact locations. The reliability of the model predictions also suggests how critical it is to properly define the external conditions of the mold in the casting simulation model.

6. CONCLUSION

The current work was a continuation of a previous study by the present authors [1]. The previous work hypothesized that the heat transfer coefficient varied locally across the external surfaces of the mold. An experimental casting trial was run with thermal couples placed in-line vertically along the blade. Analytical models were derived with the first law of thermodynamics, Newton's Law of Cooling, Fourier's Law, and diffuse gray radiation for an N-sided enclosure as the governing equations. The experimental thermocouple data was used as input to the analytical models to derive a temperature dependent emissivity expression and unique transient heat transfer coefficient expressions for each data point. The derived emissivity and local transient heat transfer coefficients were used to define the external heat conditions in the ProCAST numerical simulation model. The derived external heat transfer mechanisms were validated by comparing the predicted external mold temperatures to the thermocouple data. The model predictions agreed with the experimental data with exceptional deviation. Phenomena associated with the convective mechanism for equiaxed investment castings was uncovered by the analytical model. The phenomena can be categorized by three subjects: 1) validation of well-known investigations; 2) working theories which have been supported by this experiment; 3) pure hypothetical assumptions which require further investigation. These phenomena are summarized below.

1. Validation of well-known investigations:

   - The heat transfer coefficient depends on vertical position.
   - The heat transfer coefficient depends on surface heat flux.

2. Working theories which have been supported by this experiment:

   - For molds being flipped right-side up during the mold transfer from pre-heat oven to furnace the heat transfer coefficient increases as the distance from the axis of rotation increases.
   - The rate of change in heat transfer coefficient depends on the number of layers of insulation through a dependency on surface heat flux. The greater the number of layers the lesser the surface heat flux and in return the lesser the heat transfer coefficient.
   - The rate of change in heat transfer coefficient depends on the specific enthalpy and local mass of the alloy through a dependency on surface heat flux generated by the heat released from the alloy during solidification.
   - During the vacuum break event, there is mixed convection, and the heat transfer coefficient depends on the relative position of the local exterior mold surface with the furnace vents.
   - At the mushy-to-solid phase transition the heat transfer coefficient decreases due to the dependency of surface heat flux with local rate of change of energy.

3. Purely hypothetical assumptions which require further investigation:

    - For surfaces very close to the fixture which the mold rests upon, or other horizontal surfaces, there is a secondary flow effect caused by the combination of buoyancy forces between the mold surface and the closest horizontal surfaces resulting in an increase in heat transfer coefficient.
    - During the pump down event, the buoyancy forces driving the bulk motion along the exterior surfaces of the mold create a resistance to the pump down which results in a sheet of air molecules surrounding the mold, resulting in a continuous increase in natural convection throughout the vacuum hold events.
    - The heat transfer coefficient is somewhat sensitive to a change in temperature dependent specific enthalpy profiles within the mushy zone.

There is an extensive plan in place to further investigate all the phenomena mentioned above internally at Siemens Energy. Perhaps the most interesting phenomena is with respect to the continuous increase in heat transfer coefficient during the vacuum hold events which is assumed to be caused by a buoyancy driven resistance to the pump down of the furnace. This phenomenon alone could serve as a continuation to this work for a future publication. The authors want to reiterate the importance of defining realistic external heat conditions in the casting simulation model. The model predictions are only as good as the boundary condition definitions. The procedure and analysis presented in this study should set the precedence for how foundries derive and validate the external boundary conditions used for equiaxed investment casting solidification process modeling.

REFERENCES

[1] Olson W., Stemmler M., Fernandez E. & Kapat J. (2024). Solidification process modeling of equiaxed investment castings with transient nonuniform boundary condition definition. *Journal of Casting & Materials Engineering*, 8(1), 1–10. Doi: https://doi.org/10.7494/jcme.2024.8.1.1.

[2] Gebhart B. (1979). The 1978 Freeman scholar lecture: Buoyancy induced fluid motions characteristic of applications in technology. *Journal of Fluids Engineering*, 101(1), 5–28. Doi: https://doi.org/10.1115/1.3448735.

[3] Sanders C.J. & Holman J.P. (1972). Franz Grashof and the Grashof number. *International Journal of Heat and Mass Transfer*, 15(3), 562–563.Doi: https://doi.org/10.1016/0017-9310(72)90220-7.

[4] Ostrach S. (1953, January). *An analysis of laminar free-convection flow and heat transfer about a flat plate paralled to the direction of the generating body force*. NASA NACA-TR-1111.

[5] Sparrow E.M. & Gregg J.L. (1958). Similar solutions for free convection from a nonisothermal vertical plate. *Transactions of the American Society of Mechanical Engineers*, 80(2), 379–386.

[6] Eckert E.R.G. (1950). *Introduction to the Transfer of Heat and Mass.* McGraw-Hill, New York.

[7] Bayley F.J. (1955). An analysis of turbulent free-convection heat-transfer. *Proceedings of the Institution of Mechanical Engineers*, 169(1), 361–370. Doi: https://doi.org/10.1243/PIME_PROC_1955_169_049_02.

[8] Vliet G.C. & Ross D.C. (1975). Turbulent natural convection on upward and downward facing inclined constant heat flux surfaces. *Journal of Heat Transfer*, 97(4), 549–554. Doi: https://doi.org/10.1115/1.3450427.

[9] Raithby G.D. & Hollands K.G.T. (1976). Laminar and turbulent free convection from elliptic cylinders, with a vertical plate and horizontal circular cylinders as special cases. *Journal of Heat Transfer*, 98(1), 72–80. Doi: https://doi.org/10.1115/1.3450473.

[10] Kuehn T.H. & Goldstein R.J. (1976). Correlating equations for natural convection heat transfer between horizontal circular cylinders. *International Journal of Heat and Mass Transfer*, 19(10), 1127–1134. Doi: https://doi.org/10.1016/0017-9310(76)90145-9.

[11] Churchill S.W. & Chu H.H. (1975). Correlating equations for laminar and turbulent free convection from a horizontal cylinder. *International journal of heat and mass transfer*, 18(9), 1049–1053. Doi: https://doi.org/10.1016/0017-9310(75)90222-7.

[12] Fand R.M., Morris E.W. & Lum M. (1977). Natural convection heat transfer from horizontal cylinders to air, water and silicone oils for Rayleigh numbers between 3×10^2 and 2×10^7. *International Journal of Heat and Mass Transfer*, 20(11), 1173–1184. Doi: https://doi.org/10.1016/0017-9310(77)90126-0.

[13] Sparrow E.M. & Gregg J.L. (1956). Laminar-free-convection heat transfer from the outer surface of a vertical circular cylinder. *Transactions of the American Society of Mechanical Engineers*, 78(8), 1823–1828. Doi: https://doi.org/10.1115/1.4014194.

[14] Ede A. J. (1967). Advances in Free Convection. *Advances in Heat Transfer*, 4(C), 1–64. Doi: https://doi.org/10.1016/S0065-2717(08)70272-7.

[15] Minkowycz W. J. & Sparrow E.M. (1974). Local nonsimilar solutions for natural convection on a vertical cylinder. *Journal of Heat Transfer*, 96, 178–183. Doi: https://doi.org/10.1115/1.3450161.

[16] Sparrow E.M. & Stretton A J. (1985). Natural convection from variously oriented cubes and from other bodies of unity aspect ratio. *International Journal of Heat and Mass Transfer*, 28(4), 741–752. Doi: https://doi.org/10.1016/0017-9310(85)90224-8.

[17] Fishenden M. & Saunders O.A. (1950). *An Introduction to Heat Transfer*. Oxford University Press, London.

[18] Lloyd J.R. & Moran W.R. (1974). Natural convection adjacent to horizontal surface of various planforms. *Journal of Heat Transfer,* 96, 443–447.Doi: https://doi.org/10.1115/1.3450224.

[19] Goldstein R.J., Sparrow E.M. & Jones D.C. (1973). Natural convection mass transfer adjacent to horizontal plates. *International Journal of Heat and Mass Transfer*, 16(5), 1025–1035. Doi: https://doi.org/10.1016/0017-9310(73)90041-0.

[20] Aung W. (1987). Mixed Convection in Internal Flows. In: S. Kakaç, R.K. Shah & W. Aung (eds.), *Handbook of Single-Phase Convective Heat Transfer*, John Wiley & Sons, New York, pp. 15.1–15.51.

[21] Gebhart B. (1971). *Heat Transfer,* 2nd ed., McGraw-Hill, New York.

[22] Chen T.S., Armaly B.F. & Aung W. (1985). Mixed Convection in Laminar Boundary-layer Flow. In: S. Kakaç, W. Aung & R. Viskanta, *Natural Convection: Fundamentals and Applications*, pp. 699–725.

[23] Sparrow E.M., Eichhorn R. & Gregg J.L. (1959). Combined forced and free convection in a boundary layer flow. *Physics of Fluids*, 2(3), 319–328. Doi: https://doi.org/10.1063/1.1705928.

[24] Lloyd J.R. & Sparrow E.M. (1970). Combined forced and free convection flow on vertical surfaces. *International Journal of Heat and Mass Transfer*, 13(2), 434–438. https://doi.org/10.1016/0017-9310(70)90119-5.

[25] Chen T.S., Mucoglu A. & Sparrow E.M. (1977). Mixed convection in boundary layer flow on a horizontal plate. *Journal of Heat Transfer*, 99(1), 66–71. Doi: https:// doi.org/10.1115/1.3450657.

[26] Mori Y. & Futagami K. (1967). Forced convective heat transfer in uniformly heated horizontal tubes (2nd report, theoretical study). *International Journal of Heat and Mass Transfer*, 10(12), 1801–1813. Doi: https://doi.org/10.1016/0017-9310(67)90051-8.

[27] Ramachandran N., Armaly B F. & Chen T.S. (1987). Measurements of laminar mixed convection flow adjacent to an inclined surface. *Journal of Heat Transfer,* 109(1), pp. 146–150. Doi: https://doi.org/10.1115/1.3248035.

[28] Churchill S.W. (1977). A comprehensive correlating equation for laminar, assisting, forced and free convection. *AIChE Journal*, 23(1), 10–16. Doi: https://doi.org/10.1002/aic.690230103.